

Bridging atomic and mesoscopic length scales with  
Replica Scanning Tunneling Microscopy:  
Visualizing the intra-unit cell pair density  
modulation of superconducting FeSe at micron  
length scale

Miguel Águeda Velasco<sup>1</sup>, Jose D. Bermúdez-Pérez<sup>1,8</sup>,  
Pablo García Talavera<sup>1</sup>, Raquel Sánchez-Barquilla<sup>1</sup>,  
Jose Antonio Moreno<sup>1</sup>, Juan Schmidt<sup>2,3,4</sup>, Sergey L. Bud'ko<sup>2,3</sup>,  
Paul C. Canfield<sup>2,3</sup>, Georg Knebel<sup>5</sup>, Midori Amano Patino<sup>5</sup>,  
Gerard Lapertot<sup>5</sup>, Jacques Flouquet<sup>5</sup>, Jean Pascal Brison<sup>5</sup>,  
Dai Aoki<sup>6</sup>, Paula Giraldo-Gallo<sup>7</sup>, Jose Augusto Galvis<sup>8</sup>,  
Isabel Guillamón<sup>1</sup>, Edwin Herrera Vasco<sup>1</sup>, Hermann Suderow<sup>1\*</sup>

<sup>1</sup>Laboratorio de Bajas Temperaturas y Altos Campos Magnéticos,  
Departamento de Física de la Materia Condensada, Instituto Nicolás  
Cabrera and Condensed Matter Physics Center (IFIMAC), Unidad  
Asociada UAM-CSIC, Universidad Autónoma de Madrid, Madrid,  
E-28049, Spain.

<sup>2</sup>Department of Physics and Astronomy, Iowa State University, Iowa,  
50011, USA.

<sup>3</sup>Ames National Laboratory, Iowa State University, Iowa, 50011, USA.

<sup>4</sup>Departamento de Física, FCEyN, Universidad de Buenos Aires,  
Buenos Aires, 1428, Argentina.

<sup>5</sup>University Grenoble Alpes, CEA, Grenoble-INP, IRIG, PHELIQS,  
Grenoble, France.

<sup>6</sup>Institute for Materials Research, Tohoku University, Ibaraki, 311-1313,  
Japan.

<sup>7</sup>Department of Physics, Universidad de Los Andes, Bogotá, 111711,  
Colombia.

<sup>8</sup>School of Sciences and Engineering, Universidad del Rosario, Bogotá,  
111711, Colombia.

\*Corresponding author(s). E-mail(s): [hermann.suderow@uam.es](mailto:hermann.suderow@uam.es);

### Abstract

Scanning Tunneling Microscopy (STM) is a cornerstone technique for visualizing the electronic density of states with atomic resolution (typically below 0.1 nm). While the field of view of most STM setups extends up to a few microns, obtaining atomic resolution over these large areas is often impractical and excessively time-consuming. This is due to the need to acquire maps with a point number reaching  $10^7$  or more with a full current or conductance vs voltage curve at each point. The standard procedure is to make large scale maps and then select small regions to zoom-in for high-resolution atomic scale analysis. However, this approach fails to address a question which is often critical: Does a specific atomic-scale modulation of the electronic density of states persist over much larger, mesoscopic length scales? Here we present a new method: Replica STM (R-STM), that overcomes this limitation, allowing the study of atomic-scale phenomena up to micron length scales. We obtained new large-area STM tunneling conductance maps in  $\text{UTe}_2$  and FeSe, spanning areas over 200 nm in size. In these large scale maps we discovered signals with wavelengths significantly exceeding interatomic distances. We show that these large-wavelength signals are replicas of the underlying atomic-scale density of states modulations. R-STM leverages these replica signals to efficiently track atomic-scale features over large areas. Using this novel technique, we show that the pair density modulation discovered recently in FeSe persists with the same characteristic wavelength up to hundreds of nm length scales. R-STM provides a powerful and practical new capability for STM to compare atomic scale with micrometer scale phenomena. The proof of principle of R-STM can be extended to any other scanning probe microscopy experiment where a periodic signal is traced as a function of position.

**Keywords:** Scanning Tunneling Microscopy at low temperatures, Superconducting density of states, charge density wave, pair density wave

## 1 Introduction

The invention of the Scanning Tunneling Microscope (STM) opened an unprecedented path to the visualization of matter at atomic scale [1]. Thanks to the capability to measure the tunneling conductance with atomic precision as a function of the voltage, it also provided a completely new method to obtain the electronic density of states of materials. In addition to the atomic precision, the tunnel junction was made through vacuum, which considerably simplified previous approaches to tunneling spectroscopy using an insulating barrier [2]. The electronic density of states is directly linked to the features of the ground state at low temperatures. Examples are the gap opened around the Fermi level in superconductors, which was measured shortly after the invention of the STM [3–5], and the observation of the superconducting vortex lattice [6–8]. Other relevant features studied with STM are those associated with charge density waves [9]. More recently, spatially modulated superconductivity, where the superconducting gap

function  $\Delta_{\vec{q}}(\vec{r})$  varies periodically in space with a characteristic momentum  $\vec{q}$  which is generally larger but close to atomic lattice wavevectors, has been also addressed [10–22]. These and other studies raise a relevant question which is often difficult to address: Up to which length scale remain atomic size modulations coherent (i.e. presenting the same wavevector)?

The difficulties associating with addressing this question are mostly technical. Atomically flat terraces several  $\mu\text{m}$  large are often found in many materials. However, mapping the density of states with atomic precision requires a point density which is difficult to obtain and implies very long term measurements. For example, a usual cryogenic STM might have a bandwidth of about 10 kHz [23–25]. A full conductance vs voltage curve with, say, 200 points, often requires at least 40 ms. Mapping an area 500 nm in size with atomic precision requires, say,  $(5000)^2$  full conductance vs voltage curves [26, 27]. This requires over 11 days to complete. Often, the tip suffers an instability during the acquisition and maps need to be repeated. The process can eventually be optimized by measuring with fewer points or increasing the bandwidth. However, the bandwidth is limited by the need of a high energy resolution at low temperatures and the resonance frequency of the elements with which the microscope is built, as for example the piezotube [23–25].

One possible solution is adaptive sparse sampling, where a random matrix of points is used in an iterative procedure until a certain signal is recovered, instead of a full scanning grid [28–31]. As we will discuss below, phenomena with well-defined wavevectors in reciprocal space can be more efficiently studied with the technique proposed here, which is based on the periodicity of both, acquisition technique and signal from the sample. Completely different approaches, such as pump-probe techniques, address ultra high frequency phenomena [32, 33], which are somewhat different from the direct measurement of the electronic density of states.

On the other hand, it is well known that periodic signals present replicas at wavenumbers larger than the wavenumber of the original periodicity, if the periodic signal is sampled with another fixed periodic ramping system. Nyquist theorem states that, in order to accurately map a periodic signal with a wavenumber  $k_{signal}$ , the sampling rate  $k_S$  must be at least double the wavenumber of the target signal  $k_S \geq 2k_{signal}$ . In our case,  $k_{signal}$  can be for example  $k_{signal} = 1/a$  where  $a$  is the interatomic distance. By contrast,  $k_S$  is given by  $k_S = 1/d$  where  $d$  is the distance between points in real space, or the number of points along a line of the scan divided by the lateral size of the map. Essentially this means at least two points per atom should be taken to get atomic resolution. With a smaller point density, a signal at a smaller wavenumber,  $k_{replica}$ , is found.  $k_{replica}$  is uniquely connected to  $k_S$ , because  $k_{replica} = |k_{signal} - nk_S|$ , where  $n$  is an integer given by rounding the ratio of  $k_{signal}$  with  $k_S$  to the nearest integer,  $n = \left\lfloor \frac{k_{signal}}{k_S} \right\rfloor$  (we note that the sign of the wavenumbers can be ignored, as the Fourier transform of a periodic signal is symmetric by inversion, a peak at  $\mathbf{k}$  occurs also at  $-\mathbf{k}$ ). We can illustrate the shape in real space of replica signals and its signature in reciprocal space by an example, see Fig. 1 (here for a two-dimensional image).

In Fig. 1(a) we show a square lattice with spacing  $\lambda_{signal} = 0.38 \text{ nm}$ . In Fig. 1(b) we show its Fourier transform presenting peaks at  $k_{signal} = \frac{1}{\lambda_{signal}} = 2.6 \text{ nm}^{-1}$ .

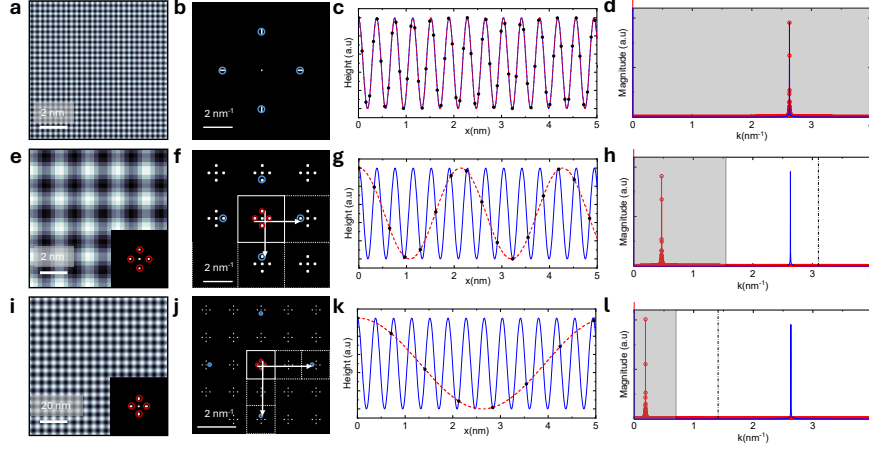


**Fig. 1 Simulated STM topography images.** A sinusoidal square lattice with spacing of 0.38 nm is sampled on three different sampling grids. **(a–d)** Fine sampling of a 10 nm  $\times$  10 nm area with 128 $\times$ 128 points. In this image,  $k_{S,0} = 12.8 \frac{1}{\text{nm}} \gg 2k_{\text{signal}} = 2 \times 2.6 \frac{1}{\text{nm}}$ . In (a) we show the sampled image. In (b) we show its Fourier transform. We find Bragg peaks at  $k_{\text{signal}}$  (blue circles). In (c) we show a line profile along the  $x$  axis. In blue we show the periodic signal. With black dots we show the points used in the image (a). The red line shows the wavefunction obtained from the black points. (d) Fourier transform of the black points (red) and of the signal (blue) of (c). **(e–h)** We now take the same square lattice and provide images using only 32 $\times$ 32 points. Now  $k_{S,1} = 3.2 \frac{1}{\text{nm}} < 2k_{\text{signal}} = 2 \times 2.6 \frac{1}{\text{nm}}$ . In (e) we show the resulting pattern, which is quite obviously periodic. In the inset of (e) we show its Fourier transform. In (f) we copy the Fourier transform of (e) several times to reach the size in reciprocal space of (b). We mark with a blue circle the Bragg peaks of the original periodicity  $k_{\text{signal}}$ . We mark with a red circle the Bragg peaks of the pattern shown in (e),  $k_{\text{replica},1}$ . Here,  $k_{\text{replica},1} = |k_{\text{signal}} - nk_{S,1}|$  with  $n = 1$ . White arrows connect red with blue peaks, as explained in the text. In (g) we show a profile along the  $x$ -axis. With a blue line we show the original periodicity. Black points show the points used in (e) and the red line joins the latter black points. In (h) we show the Fourier transform of (g). Blue points are the Fourier transform of the original signal and red points of the replica. **(i–l)** Here we enlarge field of view to 100 nm lateral size and take 128 $\times$ 128 points. Now  $k_{S,2} = 1.28 \frac{1}{\text{nm}} < 2k_{\text{signal}} = 2 \times 2.6 \frac{1}{\text{nm}}$ . We observe again a periodic pattern (i) at a wavenumber which is smaller than the wavenumber of the generating function. Its Fourier transform is shown in the lower right inset of (i). In (j) we copy the Fourier transform of (i) to obtain a similarly sized reciprocal space as in (b). The Bragg peaks corresponding to the replica,  $k_{\text{replica},2}$  are marked by red circles. The original Bragg peaks as blue circles. In (k) we show as black points the points building up the image (i) along a line. The red dashed line shows the wavefunction obtained from the black points. In blue we show the generating periodic signal. In (l) we show the Fourier transform of (k). We now have  $k_{\text{replica},2} = |k_{\text{signal}} - nk_{S,2}|$  with  $n = 2$ . We show as a grey shadow the so-called Nyquist band, given by  $\frac{k_S}{2}$ . We see that the original periodic signal at  $k_{\text{signal}}$  has a replica within the Nyquist band. As a result, one can address short length scale phenomena over large scale fields of view with undersampling grids. The periodicity of the generating signal is recovered by copying the reciprocal space area as many times as needed to cover the area required to describe the original periodic signal (at  $k_{\text{signal}}$ ) and up-folding the replica wavevector following the white arrows in (f,j; arrows are located, for clarity, slightly shifted with respect to the Bragg peaks). The white arrows are vectors  $n_{x,y}\mathbf{k}_S^{x,y}$ , with  $\mathbf{k}_S^{x,y}$  the wave vectors of the sampling unit cell in reciprocal space along  $x$  or  $y$  axis.

The square lattice has been obtained by plotting a periodic wavefunction on top of a matrix of points. The periodic wave function along the  $x$ -axis is shown in Fig. 1(c)

by the blue line. A profile along  $x$  of the point matrix (data plotted in Fig. 1(a)) is shown as black points. The red line shows the wavefunction described by the black points. In Fig. 1(d) we compare the Fourier transform of the original signal (blue in Fig. 1(c)) with the one obtained from the profile of the image in Fig. 1(c). The use of points in red shows that sampling is discrete. The map in Fig. 1(a) contains  $128 \times 128$  points and is  $10 \text{ nm} \times 10 \text{ nm}$  large. Thus, the distance in real space between black points line in Fig. 1(c) is of about  $0.078 \text{ nm}$ . There are about five points per period (black dots per period of the blue curve in Fig. 1(c)). More exactly  $k_{S,0} = 12.8 \text{ nm}^{-1}$  and  $k_{S,0} \gg 2k_{signal}$ . Most important is that the Fourier transform of the blue (original) and red (sampled) data present a peak at the same value, at  $k_{signal}$ .

We can now reduce the number of points in the map, maintaining the same wave function to generate the map. As we show in Fig. 1(e) (same lateral size but just 32 points), the result is also a periodic pattern. In this case, Nyquist theorem is not met. Here we have that  $k_{S,1} = 3.2 \text{ nm}^{-1}$ , so that  $k_{S,1} < 2k_{signal}$ . In the Fourier transform of Fig. 1(e), shown in Fig. 1(f) we find four peaks from the new pattern. These are located at a value  $k_{replica,1} < k_{signal}$ . We can understand this by looking at the original wave function, shown by a blue line in Fig. 1(g), and comparing it with the aliased wavefunction obtained from the black points in Fig. 1(g), shown as a dashed red line. We see that the red line also follows a periodic pattern, but with a much larger wavelength. The latter provides the pattern of Fig. 1(e) and the peaks in its Fourier transform (Fig. 1(f)). The Fourier transform now presents a peak at  $k_{replica,1} = |k_{signal} - nk_{S,1}|$ . In this case  $n = 1$  and  $k_{replica,1} = |2.63 - 3.2| = 0.57 \text{ nm}^{-1}$ . Using the relation between  $k_{replica,1}$  and  $k_{signal}$ , we can always identify  $k_{replica,1}$  as a consequence of the modulation at  $k_{signal}$  in a large under sampled map. Importantly, if we observe a modulation at  $k_{replica}$  in a large size map, we can deduce that the modulation at  $k_{signal}$  is present over the whole map.

We can also increase the field of view to  $100 \text{ nm} \times 100 \text{ nm}$  maintaining  $128 \times 128$  points. Now  $k_{S,2} = 1.28 \text{ nm}^{-1}$  and again  $k_{S,2} < 2k_{signal}$ . Although the map is heavily under sampled, there is a periodic pattern, as shown in Fig. 1(i). The corresponding Fourier transform (Fig. 1(j)) shows four peaks and the one-dimensional modulation shows a modulation at a very small  $k_{replica,2}$  (Fig. 1(k,l)). Now,  $n = 2$  and  $k_{replica,2} = |2.63 - 2.56| = 0.07 \text{ nm}^{-1}$ .

We can now concretely address the presence of replicas in STM images. In general, as we shall see below, we can apply the same principle to any signal on an arbitrary direction in two dimensions by translating the aliased Bragg peak along the  $x$  and  $y$  axis by an integer multiple of the sampling wavenumber on each direction,  $n_{x,y} \mathbf{k}_S^{x,y}$  and find the relationship between  $k_{replica}$  and  $k_{signal}$ . We represent these translations as white arrows in Fig. 1(f,j).

## 2 STM Methods

To perform the topographic STM and the tunneling conductance maps we use a STM setup described in Refs. [24, 25, 34, 35]. We mostly focus here on data taken from 1 K to 5 K. We use tips of PtIr, which we cut mechanically and sharpen in-situ by repeated indentation on a gold sample [36]. For the topographic images, taken in the

constant current mode, we use square grids, generally  $256 \times 256$  large. The tunneling conductance maps are obtained by acquiring full current vs voltage curves, each one of 256 points, in each point of a square grid of a similar size and subsequently taking the numerical derivative of the current vs voltage. We cleave samples in-situ using the method described in [25, 34]. In  $\text{UTe}_2$  we obtain flat surfaces which show the (011) crystallographic direction of the orthorhombic crystal structure, as in previous work [22, 37–41]. Single crystals of  $\text{UTe}_2$  were grown using the chemical vapor transport method, as described in Refs. [42, 43]. The starting materials, U and Te were sealed under vacuum in a quartz ampoule with an atomic ratio of 1:1.5 together with a transport agent iodine. The ampoule was gradually heated in a horizontal furnace, and the temperature gradient  $1050/990$  °C was applied and maintained for 10-14 days. Single crystals were obtained at the lower temperature side. FeSe crystals were obtained by vapour growth, as described in Ref. [44].

### 3 Results

#### 3.1 Atomic lattice of $\text{UTe}_2$

Let us start with the example of topographic STM measurements of the atomic lattice of  $\text{UTe}_2$ . As we show in Fig. 2(a), a map of about 50 nm in lateral size, atomic scale topography STM maps show a row-like pattern which is due to Te chains exposed after in-situ cryogenic cleaving. This image is similar to the images obtained in previous work and shows the (011) surface of the orthorhombic lattice of  $\text{UTe}_2$  [22, 37–41]. The Te atoms at the surface present a distorted hexagonal ordering which is well identified in the Fourier transform by two main wave vectors, marked in light and dark blue in Fig. 2(b). The pattern is more intricate than a simple chain, and the two wave vectors are explained by the properties of the surface crystal structure [22, 37–41]. Furthermore, there are large size atomically flat terraces. As we will see now, we can identify the Te chains in much larger images, made with the same number of points.

We show in Fig. 2(c) a map with about 100 nm lateral size. There are features in the map which provide peaks in the Fourier transform (upper right inset of Fig. 2(c)). To identify these peaks, and following the discussion above, we copy the Fourier transform as many times as needed to obtain a reciprocal space map of similar size as in the map where we observe the atomic rows (Fig. 2(b)). We find the pattern shown in Fig. 2(d). Using the vectors shown by white arrows, we can up-fold the modulations observed in Fig. 2(c), shown by light and dark red circles, to the atomic Bragg peaks (shown by light and dark blue circles). We find for the vectors highlighted in Fig. 2(d)  $\mathbf{k}_{\text{UTe}_2,1} = (0, k_S) + \mathbf{k}_{\text{replica,UTe}_2,1}$  and  $\mathbf{k}_{\text{UTe}_2,2} = (0, k_S) + (2k_S, 0) + \mathbf{k}_{\text{replica,UTe}_2,2}$ .

In an even larger map, Fig. 2(e) of nearly 200 nm size, we identify one clear peak in the Fourier transform, that corresponds to the modulation in dark blue in Fig 2(b). By repeating the steps discussed above, we obtain Fig. 2(f), and can connect the Bragg peaks observed in Fig. 2(e) to the original modulation by adding  $(2k_S, 0)$  and  $(0, k_S)$  to the replica. This shows that the Te chains occur with the same periodicity over micron length scales.

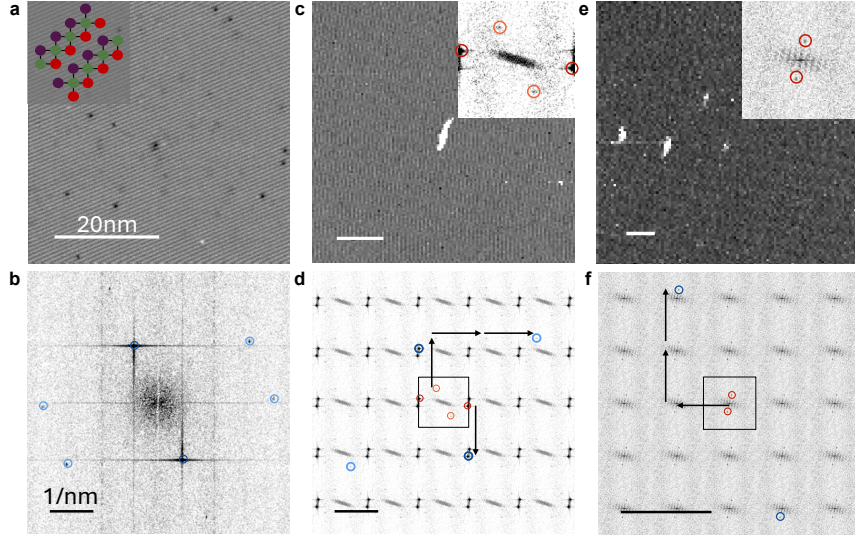


**Fig. 2 Replicas in STM topographic maps in  $\text{UTe}_2$  of different sizes.** (a) STM topography map with atomic resolution. We observe Te chains and several defects (dark spots in the image). The corresponding Fourier transform (b) shows six Bragg peaks. The two peaks with the highest intensity, marked in dark blue, correspond to the Te chains. The other Bragg peaks, in light blue, provide the distorted lattice of atoms formed by the surface cut to the bulk crystalline structure (the (011) plane, see Refs. [22, 37–41]). The Fourier transform is shown as an inset on the larger images, with red arrows indicating the aliased Te chain peaks, and blue arrows indicating the atomic periodicity along the chains. (b,d,f) Extended Fourier transform of the images in (a,c,e), respectively. Black bar is  $1\text{nm}^{-1}$  for (b,d,f). The black rectangle shows the boundaries of the downfolded reciprocal space of the image. Red and blue circles represent the true wavevectors of the Te chain and atomic lattice, respectively. Black arrows display the wavevectors used to translate the peaks from the aliased coordinates to their true positions. The white scale bar is 20nm for (a,c,e). Arrows are located, for clarity, slightly shifted with respect to the Bragg peaks ( $V_{\text{Bias}} = -50$  mV,  $I_{\text{Set}} = 200$  pA,  $T = 4.7$  K).

## 3.2 Pair Density Modulation in FeSe

### 3.2.1 Atomic scale topography of FeSe.

Having shown that atomic size topographic features are well observed as replicas in large size images, we now concentrate on maps of the tunneling conductance. We choose the paradigmatic case of FeSe, where numerous previous STM works have unveiled and analyzed spatially resolved superconducting features, including nematicity, behavior at nematic phase boundaries, vortex lattices, or, most recently, a novel pair density modulation when the inversion symmetry is broken at the surface by an enlarged  $c$ -axis constant [21, 45–54]. FeSe has a tetragonal crystal structure which becomes slightly orthorhombic below 90 K [55–57]. FeSe becomes superconducting below approximately 9 K [55, 58]. In-situ exfoliation reveals the van-der-Waals stacking along the  $c$ -axis and provides square lattices formed by Se atoms on the surface. The orthorhombicity is less than 0.5% of the in-plane crystalline lattice and essentially

indistinguishable using STM. The square Se atoms at the surface are separated by  $\approx 3.8 \text{ \AA}$ .

We observe here, as in previous works, the square Se atomic lattice by usual STM topography, as shown in Fig. 3. In Fig. 3(a) we show an image with atomic resolution presenting the usual square Se lattice, and in Fig. 3(b) we present its Fourier transform. We now enlarge the field of view in the same area, maintaining the number of points and obtain Figs. 3(c,e). The latter figures also present a periodic signal, with wave vectors that do not correspond to the square Se lattice. By making the construction described above, we connect these wave vectors with the atomic lattice adding  $(k_S, 0)$  and  $(0, k_S)$  to the replicas in the case of Figs. 3(c,d). In the case of Figs. 3(e,f) we add  $(k_S, 0)$  and  $(0, 2k_S)$ . We note that the association is unambiguous. Of course, prior knowledge of the position and size of the atomic wave vectors is required. However, the modulation shown in Figs. 3(c,e) is unambiguously due to the periodic atomic lattice, even if the image is in itself under sampled.

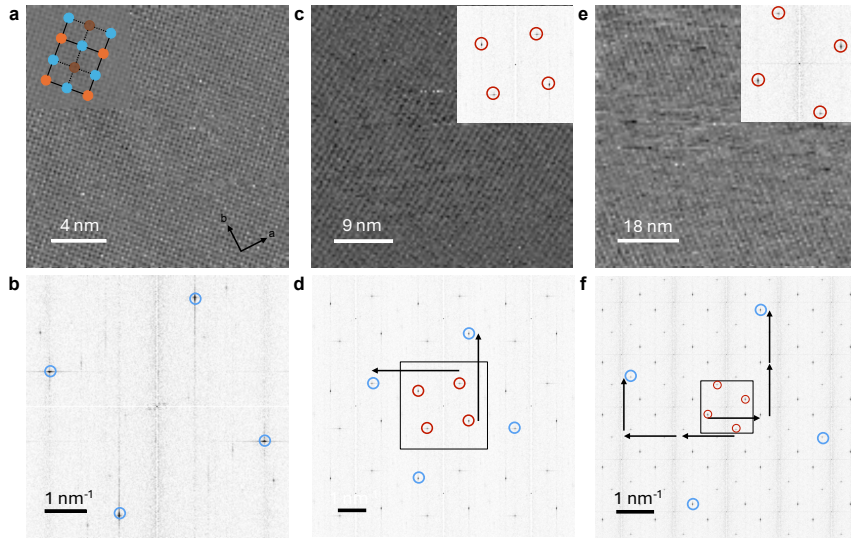


**Fig. 3** (a,c,e) STM Topographic images in FeSe with different lateral sizes and the same number of points ( $V_{\text{Bias}} = 6 \text{ mV}$ ,  $I_{\text{Set}} = 4 \text{ nA}$ ,  $T = 1 \text{ K}$ ). We show the Fourier transform of (a) in (b) and highlight with blue circles the position of the Bragg peaks of the atomic Se lattice. The Fourier transforms of (c) and (e) are shown in its upper right insets and provide also four Bragg peaks (red circles). These are located at wave vectors which are significantly smaller than the atomic Bragg peaks and with orientations which do not match directly the atomic Se lattice. In (d,f) we show the same Fourier transform, repeated in such a way as to recover an area in reciprocal space sufficiently large to represent the atomic Bragg peaks. We highlight the atomic Bragg peaks (the same as in (b)) with blue circles. The Fourier transforms of (c,e) are also marked by a black square in (d,f). Black arrows are  $\mathbf{k}_{\text{sample},x,y}$  used to up-fold the replica Bragg peaks (red circles) to the actual atomic lattice (blue circles).

### 3.2.2 Pair density modulation in layers of FeSe.

To get full advantage of the possibilities of R-STM, we now address images where we make full tunneling conductance vs bias voltage curves at each point of the image.

We focus on the pair density modulation. The pair density modulation consists of a modulation of the superconducting gap at atomic scale originated by a combination of nematicity, glide symmetry breaking and an anisotropic superconducting gap [21, 51–54]. The pair density modulation has been observed in very thin flakes of FeSe by imaging areas which are several nm of lateral size [21, 52, 53]. We present a simplified picture of the atomic and electronic structure of the surface of FeSe in Fig. 4. More details are provided in Refs. [21, 51–54, 59, 60]. The atomic structure viewed from the surface of FeSe is shown schematically in Fig. 4(a), following [21]. The upper Se atoms (orange disks in Fig. 4(a)) are mostly visible in STM topographies. As mentioned above, the orthorhombicity is very small and the nematicity is essentially an electronic property which is seen as an in-plane anisotropic Fermi surface, shown in a simplified form in Fig. 4(b). Experimentally, the distinguishing feature of the areas where a pair density modulation is observed is an enlarged c-axis constant, obtained when measuring the distance between layers on steps at the surface and observing distances approximately 20% larger than  $\delta c \approx 5.5 \text{ \AA}$  [21]. This implies that Fe atoms are located at slightly different distances from the Se planes, providing the structure shown in Fig. 4(c). This breaks the glide symmetry of the FeSe blocks. As a consequence, the Fermi surface shows the simplified structure presented in Fig. 4(d), which has two wave vectors joining the central hole pockets. According to Refs. [21, 51], this provides a spatial modulation of the amplitude of the superconducting gap. To study this feature, we focus here on situations where we observe steps close to the atomically flat areas which have heights larger than  $\delta c \approx 5.5 \text{ \AA}$  at some occasions reaching  $\delta c \approx 7 \text{ \AA}$ . These steps occur occasionally due to the in-situ mechanical exfoliation procedure, as shown for instance in Refs. [61, 62]. In these areas, we have made atomic scale maps of the tunneling conductance in the superconducting phase (Fig. 5). In images a few nm in lateral size, we essentially reproduce previous results [21, 51–53]. As we show in Fig. 5(c) there is a spatially fluctuating superconducting gap, with wave vectors coinciding with  $q_1$  and  $q_3$  in Fig. 4(d).

To address the question if such a pair density modulation is observed over large length scales, we now use R-STM. We acquire an image of over 200 nm in lateral size with just  $256 \times 256$  points (Fig. 5(d)). We have made full conductance vs bias voltage curves at each point. From the latter curves, we have built a map of the superconducting gap, at a scale of 200 nm. Its Fourier transform (Fig. 5(e)) shows clearly four peaks. These are connected to the gap modulations observed at atomic scale represented in Fig. 5(f).

To see this more clearly, we show in Fig. 6(a-d) profiles of the tunneling conductance as a function of the distance. We show the calculated relative variation of the locally observed gap size for positive and negative bias voltages in each figure ( $\delta\Delta^{+,-}$ ). We show data along the Se lattice (Fig. 6(a,c)) and along the Fe lattice (Fig. 6(b,d)). We see clearly that the corresponding modulations have a completely different wavenumber when measured with atomic precision (Fig. 6(a,b)) as compared to measurements using R-STM (Fig. 6(c,d)).

By replicating the small Fourier space of the large scale image (Fig. 5(f)) we find the original pair density modulations at  $q_1$  and  $q_3$  by adding multiples of  $k_S$  to the replicas, as shown by the white vectors in Fig. 5(g).

Thus, we see that R-STM bridges the distance between atomic size and near to micron sized modulations, and demonstrates that the recently observed pair density modulation of FeSe occurs over large length scales.

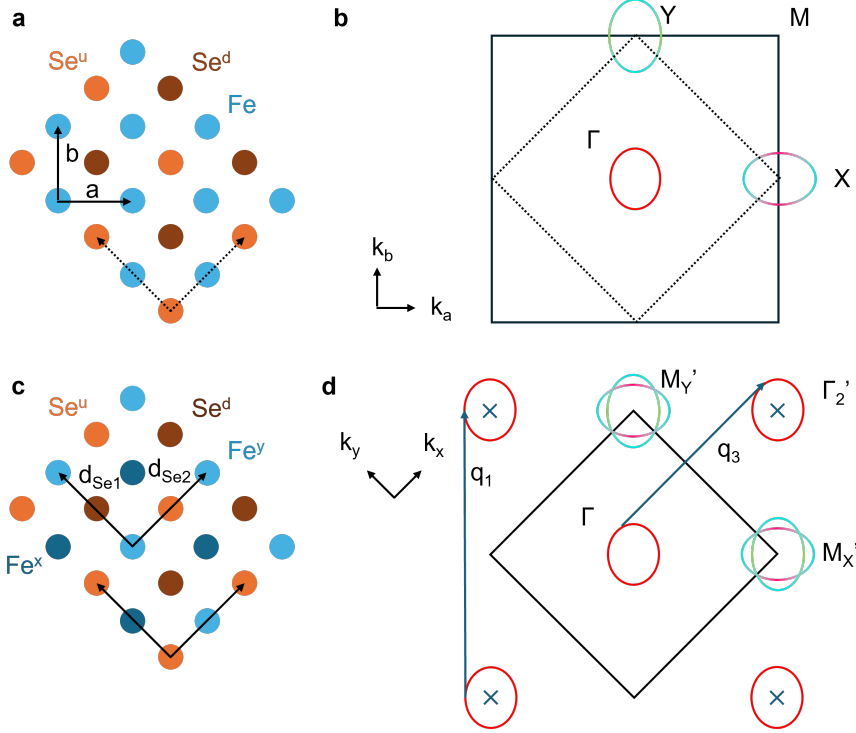


**Fig. 4 Symmetries in FeSe.**(a) We show as orange and brown disks the Se lattice, with upper labels  $^u$  and  $^d$  to indicate the upper and lower Se planes, with respect to the surface. Blue disks represent the Fe atomic lattice. In the nematic phase, the in-plane crystalline axis are slightly different (black arrows). (b) Cartoon representation of the Fermi surface of the nematic phase of FeSe in reciprocal space. We show as a black square the Brillouin zone of the Fe lattice and as a black dashed line square the Brillouin zone of the Se lattice (the two-Fe lattice unit cell, also represented in real space by dashed arrows in (a)). In the nematic phase, there is a hole-like pocket at the center of the Brillouin zone and electron-pockets at the corners. Nematicity is shown by the in-plane symmetry breaking of the electronic properties. (c) When glide symmetry is broken close to the surface, the Fe atoms are no longer equivalent. Therefore, we use dark and light blue disks for the two Fe sites. (d) We show as a black square the two-Fe unit cell. The Fermi surface is now folded and there are unit cell sized wave vectors  $q_1$  and  $q_3$  which join the central Fermi surface hole pockets into each other.

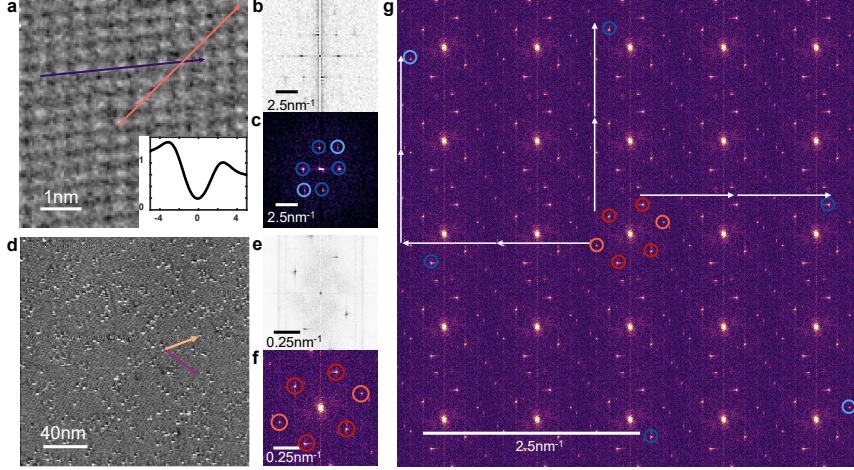


**Fig. 5 Pair density modulation observed with R-STM.** (a) Atomically resolved STM topographic image in FeSe taken at 4.2K and zero field (bias voltage of 10 mV and current of 1.2 nA). White scale bar is 1nm long. Inset shows the average tunneling conductance on the area. The corresponding data form a matrix of  $256 \times 256$  points. Points in the matrix provide the color scale, which corresponds to changes in height by about 20 pm from black to white. (b) Fourier transform of (a). Simultaneously to (a) we took maps of the tunneling conductance as a function of the bias voltage at each point. For each tunneling conductance curve, we calculated the position of the quasiparticle peak. We built a map of the position in bias voltage of the quasiparticle peaks. In (c) we show the Fourier transform of the gap magnitude. Dark and light blue circles indicate Se and Fe true Bragg peaks, respectively. (d) STM topographic image taken in FeSe at a temperature of 1 K (tunneling current of 3 nA and bias voltage of 6 mV). White bar is now 40 nm large. The matrix of this image has  $256 \times 256$  points, which implies one point every two unit cells. Locations of profiles of the tunneling conductance shown in the Fig. 6 are shown here in colored arrows. (e) Fourier transform of (d), showing clear Bragg peaks. We acquired simultaneously a tunneling conductance map. (f) Fourier transform of the gap magnitude. Dark and light orange circles indicate Se and Fe aliased Bragg peaks, respectively. (g) Same that as (f) but represented as the Extended Fourier transform. Orange circles indicate the observed aliased Bragg peaks, and blue circles their true counterparts. White arrows show the shifts used to connect both sets.

## 4 Discussion

We have shown for two different examples that R-STM is a powerful new technique to study atomic size modulations over very large length scales. The modulations can be easily identified in the Fourier transform of the images. However, we note that relevant information, as behavior at steps, or at atomic size impurities [21, 63, 64], are lost in their replicas.

It is useful to compare our technique with sparse sampling[28–31]. Both techniques aim to reduce the acquisition time of STM data, but take very different paths to achieve that. Sparse sampling is a very flexible and powerful technique for exploring large areas, and can work generally for any kind of dataset. However, the system under study has to be limited to a few narrow features in order to achieve significant time savings. On the other hand, replicas don't require the data to be sparse, but rather than it is localized as much as possible in reciprocal space, so that aliasing doesn't map different features into the same wavevectors. This means that for different kinds

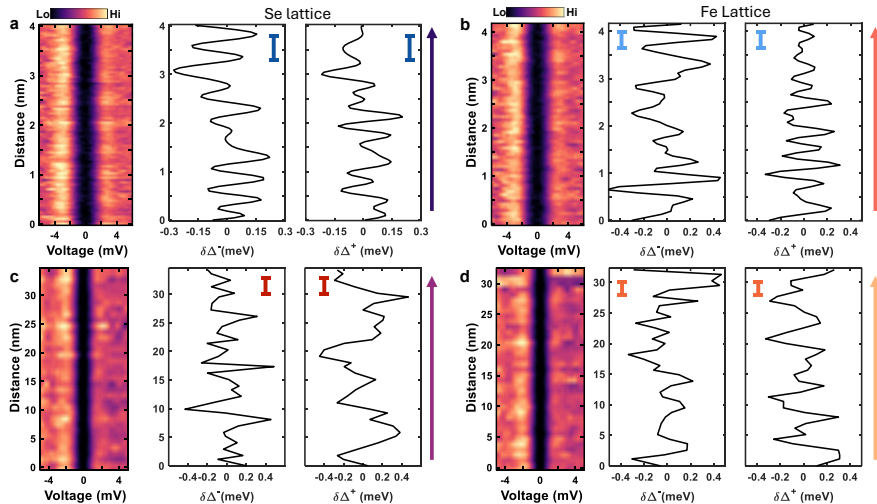


**Fig. 6** Changes of the superconducting gap in different length scales. (a) In the left panel we show with a color scale the tunneling conductance versus bias voltage along the black line shown in Fig. 5(a). In the middle and right panels we show the difference in the gap magnitude  $\delta\Delta^{+,-}$  for positive  $\delta\Delta^+$  and negative bias voltages  $\delta\Delta^-$ , obtained as discussed in the text. (b) Same along the red arrow shown in Fig. 5(a). (c,d) Same, but along the black and red arrows of Fig. 5(d). Notice the change in the length scale when comparing (a,b) with (c,d).

of datasets, one technique will perform better than the other. One significant benefit of sparse sampling is the ability to use informed sampling, tailoring the sampling pattern to the area of interest to optimize the signal. A relevant issue in sparse sampling is that it involves additional computations, both before data acquisition to calculate an optimized path for the tip, and after data acquisition[28–31]. R-STM is directly implemented in any scanning probe set-up, and even used a post-processing technique on existing data. The best results will be achieved for periodic signals and by carefully choosing the sampling frequency for the given data.

## 5 Conclusion

In conclusion, we have shown that large scale images with R-STM provide accurate information about atomic modulations at long length scales. The unequivocal association of replicas from atomic modulations can be used to demonstrate coexisting phenomena at different length scales. We can think of identifying and studying atomic density modulations and the superconducting vortex lattice at the same time, unveiling the spatial dependencies for different energies close to the Fermi level. For instance, sometimes vortex lattice images present periodic stripes at length scales which are much larger than atomic distances (for example Figure 3a in Ref. [65] or Figure 1 of Ref. [66]). It would be interesting to analyze if these stripes are due to replicas of smaller sized atomic size modulations. R-STM will be also very helpful to associate atomic size features in semimetals and semiconductors, as reconstructions or local

charge density modulations around atomic size impurities, with large scale charge density modulations[67, 68].

R-STM can be directly applied to any local probe technique, bridging length scales which are separated by many orders of magnitude as long as the relevant phenomena are characterized by small scale periodic modulations. For example, magnetic patterns in scanning magnetic techniques[69–71], electronic patterns with multiple periodicities combined with disorder[72], atomic size features in nanostructured samples[73], periodic features observed by atomic force microscopy[74], or heat dissipation patterns probed by local thermal techniques[75, 76].

**Acknowledgements.** This work was supported by the Spanish Research State Agency (PID2020-114071RB-I00, PID2023-150148OB-I00, TED2021-130546BI00 and CEX2023001316-M), Comunidad de Madrid through project TEC-2024/TEC-380 “Mag4TIC” and PhD thesis support (PIPF-2023/TEC-30853 and PIPF-2023/TEC-30683), and the EU through grant agreement No 871106. We acknowledge the QUASURF project (SI4/PJI/2024-00199) funded by the Comunidad de Madrid through the agreement to promote and encourage research and technology transfer at the Universidad Autónoma de Madrid. We acknowledge collaborations through EU program Cost CA21144 (www.superqumap.eu). We also acknowledge SEGAINVEX for support in design and for construction of the electronics of the STM.

## References

- [1] G. Binnig, H. Rohrer, Scanning tunneling microscopy—from birth to adolescence. *Rev. Mod. Phys.* **59**, 615–625 (1987). <https://doi.org/10.1103/RevModPhys.59.615>
- [2] E.L. Wolf, *Principles of Electron Tunneling Spectroscopy*, 2nd edn. International Series of Monographs on Physics (Oxford University Press, 2012)
- [3] A.L. de Lozanne, S.A. Elrod, C.F. Quate, Spatial Variations in the Superconductivity of Nb<sub>3</sub>Sn Measured by Low-Temperature Tunneling Microscopy. *Phys. Rev. Lett.* **54**, 2433–2436 (1985). <https://doi.org/10.1103/PhysRevLett.54.2433>
- [4] J.R. Kirtley, S.I. Raider, R.M. Feenstra, A.P. Fein, Spatial variation of the observed energy gap in granular superconducting NbN films. *Applied Physics Letters* **50**(22), 1607–1609 (1987). <https://doi.org/10.1063/1.97795>
- [5] H.G. Le Duc, W.J. Kaiser, J.A. Stern, Energy-gap spectroscopy of superconductors using a tunneling microscope. *Applied Physics Letters* **50**(26), 1921–1923 (1987). <https://doi.org/10.1063/1.97687>
- [6] H.F. Hess, R.B. Robinson, R.C. Dynes, J.M. Valles, J.V. Waszczak, Scanning-Tunneling-Microscope Observation of the Abrikosov Flux Lattice and the Density of States near and inside a Fluxoid. *Phys. Rev. Lett.* **62**, 214–216 (1989). <https://doi.org/10.1103/PhysRevLett.62.214>

- [7] H. Suderow, I. Guillamón, J.G. Rodrigo, S. Vieira, Imaging superconducting vortex cores and lattices with a scanning tunneling microscope. *Superconductor Science and Technology* **27**(6), 063001 (2014). <https://doi.org/10.1088/0953-2048/27/6/063001>
- [8] O. Fischer, M. Kugler, I. Maggio-Aprile, C. Berthod, C. Renner, Scanning tunneling spectroscopy of high-temperature superconductors. *Rev. Mod. Phys.* **79**, 353–419 (2007). <https://doi.org/10.1103/RevModPhys.79.353>
- [9] C.G. Slough, B. Giambattista, A. Johnson, W.W. McNairy, R.V. Coleman, Scanning tunneling microscopy of charge-density waves in NbSe<sub>3</sub>. *Phys. Rev. B* **39**, 5496–5499 (1989). <https://doi.org/10.1103/PhysRevB.39.5496>
- [10] D.F. Agterberg, J.S. Davis, S.D. Edkins, E. Fradkin, D.J. Van Harlingen, S.A. Kivelson, P.A. Lee, L. Radzihovsky, J.M. Tranquada, Y. Wang, The Physics of Pair-Density Waves: Cuprate Superconductors and Beyond. *Annual Review of Condensed Matter Physics* **11**(Volume 11, 2020), 231–270 (2020). <https://doi.org/10.1146/annurev-conmatphys-031119-050711>
- [11] Z. Du, H. Li, S.H. Joo, E.P. Donoway, J. Lee, J.C.S. Davis, G. Gu, P.D. Johnson, K. Fujita, Imaging the energy gap modulations of the cuprate pair-density-wave state. *Nature* **580**(7801), 65–70 (2020). <https://doi.org/10.1038/s41586-020-2143-x>
- [12] S. Wang, P. Choubey, Y.X. Chong, W. Chen, W. Ren, H. Eisaki, S. Uchida, P.J. Hirschfeld, J.C.S. Davis, Scattering interference signature of a pair density wave state in the cuprate pseudogap phase. *Nature Communications* **12**(1), 6087 (2021). <https://doi.org/10.1038/s41467-021-26028-x>
- [13] M.H. Hamidian, S.D. Edkins, S.H. Joo, A. Kostin, H. Eisaki, S. Uchida, M.J. Lawler, E.A. Kim, A.P. Mackenzie, K. Fujita, J. Lee, J.C.S. Davis, Detection of a Cooper-pair density wave in Bi<sub>2</sub>Sr<sub>2</sub>CaCu<sub>2</sub>O<sub>8+x</sub>. *Nature* **532**(7599), 343–347 (2016). <https://doi.org/10.1038/nature17411>
- [14] W. Chen, W. Ren, N. Kennedy, M.H. Hamidian, S. Uchida, H. Eisaki, P.D. Johnson, S.M. O’Mahony, J.C.S. Davis, Identification of a nematic pair density wave state in Bi<sub>2</sub>Sr<sub>2</sub>CaCu<sub>2</sub>O<sub>8+x</sub>. *Proceedings of the National Academy of Sciences* **119**(31), e2206481119 (2022). <https://doi.org/10.1073/pnas.2206481119>
- [15] H. Zhao, R. Blackwell, M. Thinel, T. Handa, S. Ishida, X. Zhu, A. Iyo, H. Eisaki, A.N. Pasupathy, K. Fujita, Smectic pair-density-wave order in EuRbFe<sub>4</sub>As<sub>4</sub>. *Nature* **618**(7967), 940–945 (2023). <https://doi.org/10.1038/s41586-023-06103-7>
- [16] Y. Liu, T. Wei, G. He, Y. Zhang, Z. Wang, J. Wang, Pair density wave state in a monolayer high-Tc iron-based superconductor. *Nature* **618**(7967), 934–939 (2023). <https://doi.org/10.1038/s41586-023-06072-x>

- [17] H. Chen, H. Yang, B. Hu, Z. Zhao, J. Yuan, Y. Xing, G. Qian, Z. Huang, G. Li, Y. Ye, S. Ma, S. Ni, H. Zhang, Q. Yin, C. Gong, Z. Tu, H. Lei, H. Tan, S. Zhou, C. Shen, X. Dong, B. Yan, Z. Wang, H.J. Gao, Roton pair density wave in a strong-coupling kagome superconductor. *Nature* **599**(7884), 222–228 (2021). <https://doi.org/10.1038/s41586-021-03983-5>
- [18] H. Deng, H. Qin, G. Liu, T. Yang, R. Fu, Z. Zhang, X. Wu, Z. Wang, Y. Shi, J. Liu, H. Liu, X.Y. Yan, W. Song, X. Xu, Y. Zhao, M. Yi, G. Xu, H. Hohmann, S.C. Holbæk, M. Dürrnagel, S. Zhou, G. Chang, Y. Yao, Q. Wang, Z. Guguchia, T. Neupert, R. Thomale, M.H. Fischer, J.X. Yin, Chiral kagome superconductivity modulations with residual Fermi arcs. *Nature* **632**(8026), 775–781 (2024). <https://doi.org/10.1038/s41586-024-07798-y>
- [19] Z.Q. Gao, Y.P. Lin, D.H. Lee, Pair-breaking scattering interference as a mechanism for superconducting gap modulation. *Phys. Rev. B* **110**, 224509 (2024). <https://doi.org/10.1103/PhysRevB.110.224509>
- [20] S. Sumita, M. Naka, H. Seo, Phase-modulated superconductivity via altermagnetism. *Phys. Rev. B* **112**, 144510 (2025). <https://doi.org/10.1103/3k12-2467>
- [21] L. Kong, M. Papaj, H. Kim, Y. Zhang, E. Baum, H. Li, K. Watanabe, T. Taniguchi, G. Gu, P.A. Lee, S. Nadj-Perge, Cooper-pair density modulation state in an iron-based superconductor. *Nature* **640**(8057), 55–61 (2025). <https://doi.org/10.1038/s41586-025-08703-x>
- [22] Q. Gu, J.P. Carroll, S. Wang, S. Ran, C. Broyles, H. Siddiquee, N.P. Butch, S.R. Saha, J. Paglione, J.C.S. Davis, X. Liu, Detection of a pair density wave state in UTe<sub>2</sub>. *Nature* **618**(7967), 921–927 (2023). <https://doi.org/10.1038/s41586-023-05919-7>
- [23] Y.J. Song, A.F. Otte, V. Shvarts, Z. Zhao, Y. Kuk, S.R. Blankenship, A. Band, F.M. Hess, J.A. Stroscio, Invited Review Article: A 10 mK scanning probe microscopy facility. *Review of Scientific Instruments* **81**(12), 121101 (2010). <https://doi.org/10.1063/1.3520482>
- [24] F. Martín-Vega, V. Barrena, R. Sánchez-Barquilla, M. Fernández-Lomana, J. Benito Llorens, B. Wu, A. Fente, D. Perconte Duplain, I. Horcas, R. López, J. Blanco, J.A. Higuera, S. Mañas-Valero, N.H. Jo, J. Schmidt, P.C. Canfield, G. Rubio-Bollinger, J.G. Rodrigo, E. Herrera, I. Guillamón, H. Suderow, Simplified feedback control system for scanning tunneling microscopy. *Review of Scientific Instruments* **92**(10), 103705 (2021). <https://doi.org/10.1063/5.0064511>
- [25] M. Fernández-Lomana, B. Wu, F. Martín-Vega, R. Sánchez-Barquilla, R. Álvarez Montoya, J.M. Castilla, J. Navarrete, J.R. Marijuan, E. Herrera, H. Suderow, I. Guillamón, Millikelvin scanning tunneling microscope at 20/22 T with a graphite enabled stick–slip approach and an energy resolution below 8  $\mu$ eV: Application to conductance quantization at 20 T in single atom point contacts of Al and

- Au and to the charge density wave of 2H-NbSe<sub>2</sub>. *Review of Scientific Instruments* **92**(9), 093701 (2021). <https://doi.org/10.1063/5.0059394>
- [26] J.E. Hoffman, K. McElroy, D.H. Lee, K.M. Lang, H. Eisaki, S. Uchida, J.C. Davis, Imaging Quasiparticle Interference in Bi<sub>2</sub>Sr<sub>2</sub>CaCu<sub>2</sub>O<sub>8+x</sub>. *Science* **297**(5584), 1148–1151 (2002). <https://doi.org/10.1126/science.1072640>
- [27] J.E. Hoffman, E.W. Hudson, K.M. Lang, V. Madhavan, H. Eisaki, S. Uchida, J.C. Davis, A Four Unit Cell Periodic Pattern of Quasi-Particle States Surrounding Vortex Cores in Bi<sub>2</sub>Sr<sub>2</sub>CaCu<sub>2</sub>O<sub>8+x</sub>. *Science* **295**(5554), 466–469 (2002). <https://doi.org/10.1126/science.1066974>
- [28] Y. Nakanishi-Ohno, M. Haze, Y. Yoshida, K. Hukushima, Y. Hasegawa, M. Okada, Compressed Sensing in Scanning Tunneling Microscopy/Spectroscopy for Observation of Quasi-Particle Interference. *Journal of the Physical Society of Japan* **85**(9), 093702 (2016). <https://doi.org/10.7566/JPSJ.85.093702>
- [29] J. Oppliger, F.D. Natterer, Sparse sampling for fast quasiparticle-interference mapping. *Phys. Rev. Res.* **2**, 023117 (2020). <https://doi.org/10.1103/PhysRevResearch.2.023117>
- [30] B. Zengin, J. Oppliger, D. Liu, L. Niggli, T. Kurosawa, F.D. Natterer, Fast spectroscopic mapping of two-dimensional quantum materials. *Phys. Rev. Res.* **3**, L042025 (2021). <https://doi.org/10.1103/PhysRevResearch.3.L042025>
- [31] J. Oppliger, B. Zengin, D. Liu, K. Hauser, C. Witteveen, F. von Rohr, F.D. Natterer, Adaptive sparse sampling for quasiparticle interference imaging. *MethodsX* **9**, 101784 (2022). <https://doi.org/10.1016/j.mex.2022.101784>
- [32] W.M.J. van Weerdenburg, M. Steinbrecher, N.P.E. van Mullekom, J.W. Gerritsen, H. von Allwörden, F.D. Natterer, A.A. Khajetoorians, A scanning tunneling microscope capable of electron spin resonance and pump-probe spectroscopy at mK temperature and in vector magnetic field. *Review of Scientific Instruments* **92**(3), 033906 (2021). <https://doi.org/10.1063/5.0040011>
- [33] S. Loth, K. von Bergmann, M. Ternes, A.F. Otte, C.P. Lutz, A.J. Heinrich, Controlling the state of quantum spins with electric currents. *Nature Physics* **6**(5), 340–344 (2010). <https://doi.org/10.1038/nphys1616>
- [34] H. Suderow, I. Guillamon, S. Vieira, Compact very low temperature scanning tunneling microscope with mechanically driven horizontal linear positioning stage. *Review of Scientific Instruments* **82**(3), 033711 (2011). <https://doi.org/10.1063/1.3567008>
- [35] J.A. Galvis, E. Herrera, I. Guillamón, J. Azpeitia, R.F. Lucas, C. Munuera, M. Cuenca, J.A. Higuera, N. Díaz, M. Pazos, M. García-Hernandez, A. Buendía, S. Vieira, H. Suderow, Three axis vector magnet set-up for cryogenic scanning

- probe microscopy. *Review of Scientific Instruments* **86**(1), 013706 (2015). <https://doi.org/10.1063/1.4905531>
- [36] J.G. Rodrigo, H. Suderow, S. Vieira, E. Bascones, F. Guinea, Superconducting nanostructures fabricated with the scanning tunneling microscope. *Journal of Physics: Condensed Matter* **16**(34), R1151 (2004). <https://doi.org/10.1088/0953-8984/16/34/R01>
- [37] P.G. Talavera, M. Águeda Velasco, M. Shimizu, B. Wu, G. Knebel, M.A. Patino, G. Lapertot, J. Flouquet, J.P. Brison, D. Aoki, Y. Yanase, E. Herrera, I. Guillamón, H. Suderow. Surface charge density wave in  $UTe_2$  (2025). <https://doi.org/10.48550/arXiv.2504.12505>
- [38] A. Aishwarya, J. May-Mann, A. Raghavan, L. Nie, M. Romanelli, S. Ran, S.R. Saha, J. Paglione, N.P. Butch, E. Fradkin, V. Madhavan, Magnetic-field-sensitive charge density waves in the superconductor  $UTe_2$ . *Nature* **618**(7967), 928–933 (2023). <https://doi.org/10.1038/s41586-023-06005-8>
- [39] A. Aishwarya, J. May-Mann, A. Almoalem, S. Ran, S.R. Saha, J. Paglione, N.P. Butch, E. Fradkin, V. Madhavan, Melting of the charge density wave by generation of pairs of topological defects in  $UTe_2$ . *Nature Physics* **20**(6), 964–969 (2024). <https://doi.org/10.1038/s41567-024-02429-9>
- [40] A. LaFleur, H. Li, C.E. Frank, M. Xu, S. Cheng, Z. Wang, N.P. Butch, I. Zeljkovic, Inhomogeneous high temperature melting and decoupling of charge density waves in spin-triplet superconductor  $UTe_2$ . *Nature Communications* **15**(1), 4456 (2024). <https://doi.org/10.1038/s41467-024-48844-7>
- [41] Q. Gu, S. Wang, J.P. Carroll, K. Zhussupbekov, C. Broyles, S. Ran, N.P. Butch, J.A. Horn, S. Saha, J. Paglione, X. Liu, J.C.S. Davis, D.H. Lee, Pair wave function symmetry in  $UTe_2$  from zero-energy surface state visualization. *Science* **388**(6750), 938–944 (2025). <https://doi.org/10.1126/science.adk7219>
- [42] D. Aoki, J.P. Brison, J. Flouquet, K. Ishida, G. Knebel, Y. Tokunaga, Y. Yanase, Unconventional superconductivity in  $UTe_2$ . *Journal of Physics: Condensed Matter* **34**(24), 243002 (2022). <https://doi.org/10.1088/1361-648X/ac5863>
- [43] S. Ran, C. Eckberg, Q.P. Ding, Y. Furukawa, T. Metz, S.R. Saha, I.L. Liu, M. Zic, H. Kim, J. Paglione, N.P. Butch, Nearly ferromagnetic spin-triplet superconductivity. *Science* **365**(6454), 684–687 (2019). <https://doi.org/10.1126/science.aav8645>
- [44] A.E. Böhmer, V. Taufour, W.E. Straszheim, T. Wolf, P.C. Canfield, Variation of transition temperatures and residual resistivity ratio in vapor-grown  $FeSe$ . *Phys. Rev. B* **94**, 024526 (2016). <https://doi.org/10.1103/PhysRevB.94.024526>

- [45] P.O. Sprau, A. Kostin, A. Kreisel, A.E. Böhmer, V. Taufour, P.C. Canfield, S. Mukherjee, P.J. Hirschfeld, B.M. Andersen, J.C.S. Davis, Discovery of orbital-selective Cooper pairing in FeSe. *Science* **357**(6346), 75–80 (2017). <https://doi.org/10.1126/science.aal1575>
- [46] K. Bu, W. Zhang, Y. Fei, Y. Zheng, F. Ai, Z. Wu, Q. Wang, H. Wo, J. Zhao, Y. Yin, Observation of an electronic order along [110] direction in FeSe. *Nature Communications* **12**(1), 1385 (2021). <https://doi.org/10.1038/s41467-021-21318-w>
- [47] T. Hanaguri, K. Iwaya, Y. Kohsaka, T. Machida, T. Watashige, S. Kasahara, T. Shibauchi, Y. Matsuda, Two distinct superconducting pairing states divided by the nematic end point in FeSe<sub>1-x</sub>S<sub>x</sub>. *Science Advances* **4**(5), eaar6419 (2018). <https://doi.org/10.1126/sciadv.aar6419>
- [48] T. Watashige, Y. Tsutsumi, T. Hanaguri, Y. Kohsaka, S. Kasahara, A. Furusaki, M. Sigrist, C. Meingast, T. Wolf, H.v. Löhneysen, T. Shibauchi, Y. Matsuda, Evidence for Time-Reversal Symmetry Breaking of the Superconducting State near Twin-Boundary Interfaces in FeSe Revealed by Scanning Tunneling Spectroscopy. *Phys. Rev. X* **5**, 031022 (2015). <https://doi.org/10.1103/PhysRevX.5.031022>
- [49] S. Kasahara, H. Suzuki, T. Machida, Y. Sato, Y. Ukai, H. Murayama, S. Suetsugu, Y. Kasahara, T. Shibauchi, T. Hanaguri, Y. Matsuda, Quasiparticle Nodal Plane in the Fulde-Ferrell-Larkin-Ovchinnikov State of FeSe. *Phys. Rev. Lett.* **127**, 257001 (2021). <https://doi.org/10.1103/PhysRevLett.127.257001>
- [50] J.E. Hoffman, Spectroscopic scanning tunneling microscopy insights into Fe-based superconductors. *Reports on Progress in Physics* **74**(12), 124513 (2011). <https://doi.org/10.1088/0034-4885/74/12/124513>
- [51] M. Papaj, L. Kong, S. Nadj-Perge, P.A. Lee. Pair density modulation from glide symmetry breaking and nematic superconductivity (2025). <https://doi.org/10.48550/arXiv.2506.19903>
- [52] Y. Zhang, L. Yang, C. Liu, W. Zhang, Y.S. Fu. Visualizing uniform lattice-scale pair density wave in single-layer FeSe/SrTiO<sub>3</sub> films (2024). <https://doi.org/10.48550/arXiv.2406.05693>
- [53] T. Wei, Y. Liu, W. Ren, Z. Liang, Z. Wang, J. Wang, Observation of Superconducting Pair Density Modulation within Lattice Unit Cell. *Chinese Physics Letters* **42**(2), 027404 (2025). <https://doi.org/10.1088/0256-307X/42/2/027404>
- [54] P.J. Chen, P. Coleman. A Landau Theory for Pair Density Modulation in Fe(Te,Se) flakes (2025). <https://doi.org/10.48550/arXiv.2512.06152>
- [55] L. Xiang, U.S. Kaluarachchi, A.E. Böhmer, V. Taufour, M.A. Tanatar, R. Prozorov, S.L. Bud'ko, P.C. Canfield, Dome of magnetic order inside the nematic

- phase of sulfur-substituted FeSe under pressure. *Phys. Rev. B* **96**, 024511 (2017). <https://doi.org/10.1103/PhysRevB.96.024511>
- [56] S.H. Baek, D.V. Efremov, J.M. Ok, J.S. Kim, J. van den Brink, B. Büchner, Orbital-driven nematicity in FeSe. *Nature Materials* **14**(2), 210–214 (2015). <https://doi.org/10.1038/nmat4138>
- [57] T.M. McQueen, A.J. Williams, P.W. Stephens, J. Tao, Y. Zhu, V. Ksenofontov, F. Casper, C. Felser, R.J. Cava, Tetragonal-to-Orthorhombic Structural Phase Transition at 90 K in the Superconductor Fe<sub>1.01</sub>Se. *Phys. Rev. Lett.* **103**, 057002 (2009). <https://doi.org/10.1103/PhysRevLett.103.057002>
- [58] A.E. Böhrer, A. Kreisel, Nematicity, magnetism and superconductivity in FeSe. *Journal of Physics: Condensed Matter* **30**(2), 023001 (2017). <https://doi.org/10.1088/1361-648X/aa9caa>
- [59] R.M. Fernandes, A.V. Chubukov, Low-energy microscopic models for iron-based superconductors: a review. *Reports on Progress in Physics* **80**(1), 014503 (2016). <https://doi.org/10.1088/1361-6633/80/1/014503>
- [60] A. Kreisel, P.J. Hirschfeld, B.M. Andersen, On the Remarkable Superconductivity of FeSe and Its Close Cousins. *Symmetry* **12**(9) (2020). <https://doi.org/10.3390/sym12091402>
- [61] J.A. Galvis, P. Rodière, I. Guillamon, M.R. Osorio, J.G. Rodrigo, L. Cario, E. Navarro-Moratalla, E. Coronado, S. Vieira, H. Suderow, Scanning tunneling measurements of layers of superconducting 2H-TaSe<sub>2</sub>: Evidence for a zero-bias anomaly in single layers. *Phys. Rev. B* **87**, 094502 (2013). <https://doi.org/10.1103/PhysRevB.87.094502>
- [62] G. Li, A. Luican, E.Y. Andrei, Scanning Tunneling Spectroscopy of Graphene on Graphite. *Phys. Rev. Lett.* **102**, 176804 (2009). <https://doi.org/10.1103/PhysRevLett.102.176804>
- [63] E. Herrera, V. Barrena, I. Guillamón, J.A. Galvis, W.J. Herrera, J. Castilla, D. Aoki, J. Flouquet, H. Suderow, 1D charge density wave in the hidden order state of URu<sub>2</sub>Si<sub>2</sub>. *Communications Physics* **4**(1), 98 (2021). <https://doi.org/10.1038/s42005-021-00598-0>
- [64] E. Herrera, I. Guillamón, V. Barrena, W.J. Herrera, J.A. Galvis, A.L. Yeyati, J. Rusz, P.M. Oppeneer, G. Knebel, J.P. Brison, J. Flouquet, D. Aoki, H. Suderow, Quantum-well states at the surface of a heavy-fermion superconductor. *Nature* **616**(7957), 465–469 (2023). <https://doi.org/10.1038/s41586-023-05830-1>
- [65] R. Bisset, L.C. Rhodes, H. Decitre, M.J. Neat, A. Maldonado, A. Huxley, C.A. Marques, P. Wahl. Determining the superconducting order parameter of UPt<sub>3</sub> using scanning tunneling microscopy (2025). <https://doi.org/10.48550/arXiv>

- [66] N. Sharma, M. Toole, J. McKenzie, F. Cheng, M.M. Bordelon, S.M. Thomas, P.F.S. Rosa, Y.T. Hsu, X. Liu, Observation of persistent zero modes and superconducting vortex doublets in  $\text{UTe}_2$ . *ACS Nano* **19**(35), 31539–31550 (2025). <https://doi.org/10.1021/acsnano.5c08406>
- [67] A. Fente, A. Correa-Orellana, A.E. Böhmer, A. Kreyssig, S. Ran, S.L. Bud'ko, P.C. Canfield, F.J. Mompean, M. García-Hernández, C. Munuera, I. Guillamón, H. Suderow, Direct visualization of phase separation between superconducting and nematic domains in Co-doped  $\text{CaFe}_2\text{As}_2$  close to a first-order phase transition. *Phys. Rev. B* **97**, 014505 (2018). <https://doi.org/10.1103/PhysRevB.97.014505>
- [68] K.A. Yay, W.J. Meese, E. Kisiel, M.J. Krogstad, A.G. Singh, R.M. Fernandes, Z. Islam, I.R. Fisher. Discovery of spontaneous mesoscopic strain waves in nematic domains using dark-field X-ray microscopy (2025). <https://doi.org/10.48550/arXiv.2507.23752>
- [69] Y. Zur, A. Noah, C. Boix-Constant, S. Mañas-Valero, N. Fridman, R. Rama-Eiroa, M.E. Huber, E.J.G. Santos, E. Coronado, Y. Anahory, Magnetic imaging and domain nucleation in  $\text{CrSb}$  down to the 2D limit. *Advanced Materials* **35**(47), 2307195 (2023). <https://doi.org/https://doi.org/10.1002/adma.202307195>
- [70] N. Auerbach, S. Dutta, M. Uzan, Y. Vituri, Y. Zhou, A.Y. Meltzer, S. Grover, T. Holder, P. Emanuel, M.E. Huber, Y. Myasoedov, K. Watanabe, T. Taniguchi, Y. Oreg, E. Berg, E. Zeldov, Isospin magnetic texture and intervalley exchange interaction in rhombohedral tetralayer graphene. *Nature Physics* **21**(11), 1765–1772 (2025). <https://doi.org/10.1038/s41567-025-03035-z>
- [71] R. Brüning, L. Rózsa, R. Lo Conte, A. Kubetzka, R. Wiesendanger, K. von Bergmann, Topological meron-antimeron domain walls and skyrmions in a low-symmetry system. *Phys. Rev. X* **15**, 021041 (2025). <https://doi.org/10.1103/PhysRevX.15.021041>
- [72] B. Jäck, F. Zinser, E.J. König, S.N.P. Wissing, A.B. Schmidt, M. Donath, K. Kern, C.R. Ast, Visualizing the multifractal wave functions of a disordered two-dimensional electron gas. *Phys. Rev. Res.* **3**, 013022 (2021). <https://doi.org/10.1103/PhysRevResearch.3.013022>
- [73] S.h. Phark, B. Weber, Y. Yoshida, P.R. Forrester, R.J.G. Elbertse, J.A. Stroschio, H. Wang, K. Yang, L. Gross, S. Mishra, F. Paschke, K. Kaiser, S. Fatayer, J. Repp, H.L. Anderson, D. Peña, F. Albrecht, F.J. Giessibl, R. Fasel, J. Fernández-Rossier, S. Kawai, L. Limot, N. Lorente, B. Jäck, H. Huang, J. Ankerhold, C.R. Ast, M. Trahms, C.B. Winkelmann, K.J. Franke, M.O. Soldini, G. Wagner, T. Neupert, F. Küster, S. Das, S.S.P. Parkin, P. Sessi, Z. Wang, V. Madhavan, R. Huber, G. Singh, F. Donati, S. Rusponi, H. Brune, E. Moreno-Pineda,

- M. Ruben, W. Wernsdorfer, W. Huang, K.H. Au-Yeung, P. Willke, A.J. Heinrich, S. Baumann, S. Loth, L.M. Veldman, S. Otte, C. Wolf, L. Sellies, S.R. Schofield, M.E. Flatté, J.G. Keizer, M.Y. Simmons, Roadmap on atomically-engineered quantum platforms. *Nano Futures* **9**(3), 032001 (2025). <https://doi.org/10.1088/2399-1984/ade6b7>
- [74] F.J. Giessibl, Advances in atomic force microscopy. *Rev. Mod. Phys.* **75**, 949–983 (2003). <https://doi.org/10.1103/RevModPhys.75.949>
- [75] D. Halbertal, J. Cuppens, M.B. Shalom, L. Embon, N. Shadmi, Y. Anahory, H.R. Naren, J. Sarkar, A. Uri, Y. Ronen, Y. Myasoedov, L.S. Levitov, E. Joselevich, A.K. Geim, E. Zeldov, Nanoscale thermal imaging of dissipation in quantum systems. *Nature* **539**(7629), 407–410 (2016). <https://doi.org/10.1038/nature19843>
- [76] J.D. Bermúdez-Perez, E. Herrera-Vasco, J. Casas-Salgado, H.A. Castelblanco, K. Vega-Bustos, G. Cardenas-Chirivi, O.L. Herrera-Sandoval, H. Suderow, P. Giraldo-Gallo, J.A. Galvis, High-resolution scanning tunneling microscope and its adaptation for local thermopower measurements in 2D materials. *Ultramicroscopy* **261**, 113963 (2024). <https://doi.org/10.1016/j.ultramic.2024.113963>